



Universidad Autónoma  
de Madrid

**Biblos-e Archivo**  
Repositorio Institucional UAM

**Repositorio Institucional de la Universidad Autónoma de Madrid**

<https://repositorio.uam.es>

Esta es la **versión de autor** del artículo publicado en:  
This is an **author produced version** of a paper published in:

Analytica Chimica Acta 1182. (2021): 338940

**DOI:** <https://doi.org/10.1016/j.aca.2021.338940>

**Copyright:** © 2021 Elsevier B.V. This manuscript version is made available under the CC-BY-NC-ND 4.0 licence <http://creativecommons.org/licenses/by-nc-nd/4.0/>

El acceso a la versión del editor puede requerir la suscripción del recurso  
Access to the published version may require subscription

# **A supramolecular hybrid sensor based on cucurbit[8]uril, 2D-molibdenum disulphide and diamond nanoparticles towards methyl viologen analysis**

Elías Blanco<sup>a</sup>, Laura Rocha<sup>a</sup>, María del Pozo<sup>a</sup>, Luis Vázquez<sup>b</sup>, María Dolores Petit-Domínguez<sup>a</sup>, Elena Casero<sup>a</sup>, Carmen Quintana<sup>a\*</sup>

<sup>a</sup>Departamento de Química Analítica y Análisis Instrumental. Facultad de Ciencias. c/ Francisco Tomás y Valiente, N°7. Campus de Excelencia de la Universidad Autónoma de Madrid. 28049 Madrid. Spain.

<sup>b</sup>ESISNA group, Instituto de Ciencia de Materiales de Madrid (CSIC). c/ Sor Juana Inés de la Cruz N°3. Campus de Excelencia de la Universidad Autónoma de Madrid. 28049 Madrid. Spain

\*Corresponding author email: carmen.quintana@uam.es

## **Abstract**

We develop an electrochemical sensor by using 2D-transition metal dichalcogenides (TMD), specifically MoS<sub>2</sub>, and nanoparticles stabilized with cucurbit[8]uril (CB[8]) incorporated together with them. Two different nanoparticles are assayed: diamond nanoparticles (DNPs) and gold nanoparticles (AuNp). 0D materials, together with TMD, provide increased conductivity and active surface while the macrocycle CB[8] affords selectivity towards the guest methyl viologen (MV<sup>2+</sup>), also named paraquat. Glassy Carbon (GC) electrodes are modified by drop-casting of suspensions of MoS<sub>2</sub>, followed by either a CB[8]-DNPs hybrid dispersion or a CB[8]-AuNp suspension. Atomic force microscopy is employed for the morphological characterization of the electrochemical sensor surface while cyclic voltammetry and electrochemical impedance spectroscopy techniques allow the electrochemical characterization of the sensor. The well-established signals of CB[8]-encapsulated MV<sup>2+</sup> arise in voltammetric measurements when the macrocycle modifies the 0D-materials. Once the sensor construction and differential

pulse voltammetry parameters have been optimized for quantification purposes, calibration procedures are performed with the platform GC/MoS<sub>2</sub>/CB[8]-DNPs. This sensing platform shows linear relations between peak intensity and the MV<sup>2+</sup> concentration in the linear concentration range of (0.73 – 8.0) · 10<sup>-6</sup> M with a limit of detection of 2.2 · 10<sup>-7</sup> M. Analyses of river water samples fortified with MV<sup>2+</sup> at the μM level shows recoveries of 100% with RSD values of 6.4 % (n = 3).

**Keywords:** Molybdenum disulphide, diamond nanoparticles, cucurbit[8]uril, methyl viologen, supramolecular chemistry.

## 1. Introduction

Chemical sensors based on supramolecular recognition incorporate, in the sensing layer, a host that generates a measurable signal upon guest recognition. Although cyclodextrins are still displaying their capabilities in sensor constructions, cucurbit[n]urils (CB[n]) have emerged as a powerful alternative from the beginning of this century [1]. CB[n] are pumpkin-shaped cyclic polymeric compounds composed of n (n= 5-10) glycoluryl units and have two symmetrical portals delimited by carbonyl oxygen atoms, which allow guests to be accommodated into the hydrophobic cavity [2]. The chemical nature of the portals, the hydrophobic cavity and the host size are responsible of the CB[n] selectivity to certain guests such as phenols, the amino acid tryptophan and the neurotransmitter dopamine [3,4], among others.

Furthermore, 2D-, 1D- or 0D-nanoarchitectures made of different materials have been functionalized with macrocycles, such as cyclodextrins and CB[n]s, for different applications. In these hybrid systems, the nanomaterial provides properties like high active surface, hardness, electric conductivity, or chemical stability while the host keeps

the well-established supramolecular recognition capability exhibited in solution. In the literature, there are examples of macrocycle-modified carbon-based nanomaterials such as graphene and its oxide [5–7], nanotubes [8] and nanoparticles [9]. There are also examples of macrocycle-modified 1D-materials made of clays or gold [10]. Likewise, gold nanoparticles (AuNp) have been modified with macrocycles for the evaluation of CB[n] complexes dissociation constants [11], catalysis [12], synergistic chemophotothermal therapy for cancer [13] and chemical analysis [14,15].

In addition to these advances, two relatively new nanomaterials, namely 2D-transition metal dichalcogenides (TMD) and 0D-diamond nanoparticles (DNPs), are gaining attention due to their interesting properties and promising applications. TMD are materials characterized by an X-M-X (X = chalcogenide, M = metal) structure in each layer, with the TMD layers being weakly bonded between them by van der Waals forces. Therefore, their top-down synthesis approach from the bulk counterparts is easily performed by, for example, ultrasounds-mediated liquid phase exfoliation in appropriate solvents, such as mixtures of ethanol and water. Their large specific surface area and semiconducting character make them apposite to be included in electrochemical designs. Thus, the dichalcogenide MoS<sub>2</sub> has been applied for the oxygen reduction reaction [16] and the hydrogen evolution [17]. In addition, applications in nanophotonics and chemical sensing have been proposed [18, 19]. On the other hand, DNPs are commercially available and have a non-conducting core of sp<sup>3</sup> carbon while the surface is composed of amorphous carbon with oxygen functionalities responsible of their electrocatalytic properties. They are non-toxic and can be used in fluorescence applications, polymer composites and as lubricants [20]. Compared with other carbon forms such as boron-doped diamond, DNPs are clearly an emerging nanomaterial in the electrochemical field where they have demonstrated their excellent properties [21,22].

Viologen-containing molecules are guests of the macrocycles CB[7] and CB[8] and have been successfully used in rotaxanes [23], biological [24] and sensing applications [25]. Methyl viologen ( $MV^{2+}$ ) is a non-selective contact herbicide known as paraquat in agricultural and toxicological fields and its efficiency and low cost have boosted its usage despite its toxicity for organisms. In the human beings, it generates an inflammatory response, harms different viscera such as heart, kidney and liver, as well as the neural system, being also associated with the Parkinson disease [26–28]. Many countries have banned it but it is still in use in more than 100 countries such as China, USA, Australia, Japan, Argentina and Taiwan, even with an increased use [26, 29–31]. From the environmental point of view, paraquat is highly resistant to microbial and chemical degradation with a half-life higher than two years [26–28,32] and, because of its high water solubility, its use can cause the pollution of water bodies and tap water [27,32,33]. Methods to analyse paraquat include: liquid chromatography [34], fluorescence [35], chemiluminescence [36], chromogenic sprays for thin-layer chromatographic analysis [37], immunochromatographic strips [27] and, also, electroanalysis [28,32,38–41].

Despite the recognition capability of CB[7] and CB[8] towards  $MV^{2+}$  and the need of  $MV^{2+}$  chemical analysis because of its wide use and high toxicity, CB[n]-modified electrochemical sensors facing  $MV^{2+}$  have been scarcely investigated in comparison with analytical methodologies that include CB[n] for other analytes [5,25]. In addition, and in the best of our knowledge, the modification of DNPs by CB[n]s has never been explored and no work has studied the use of these macrocycles and 2D-TMD in the same device. Therefore, this work proposes to develop an electrochemical sensor that takes the advantages in sensitivity of the use of 2D-TMD and 0D-nanoparticles (i.e. AuNp and DNPs) together with the selectivity derived from the molecular recognition properties of CB[n] ( $n = 7, 8$ ) that are anchored to the 0D-elements. Because  $MV^{2+}$  is a harmful and

still used herbicide, the analytical performance of this supramolecular platform will be evaluated to determine  $MV^{2+}$  in river water samples.

## **2. Materials and methods**

### **2.1. Reagents**

Molybdenum disulfide ( $MoS_2$ , 90 nm powder), cucurbit[n]urils (CB[n],  $n = 7, 8$ ), methyl viologen dichloride hydrate ( $MV^{2+} \cdot 2 Cl^- \cdot H_2O$ ), 5 nm-gold nanoparticles stabilized in citrate buffer, hexaammineruthenium(II) chloride, 4,4'-oxydianiline (Oxy), thiabendazole (Tbz) and carbendazim (Cbz) all 99% were obtained from Sigma Aldrich (St. Louis, MO, USA). Diamond nanoparticles (DNPs) were obtained from SkySpring Nanomaterials, Inc (Houston, Texas, USA). Phosphoric, acetic and boric acids, potassium chloride, ethanol absolute (EtOH) and sodium hydroxide were purchased from Scharlab (Senmanat, Spain). Sodium borohydride ( $NaBH_4$ ) and tetrachloroauric(III) acid trihydrate ( $HAuCl_4 \cdot 3 H_2O$ ) were obtained from Riedel-de Haën (Seelze, Germany) and Across Organics (Geel, Belgium), respectively. Nippon Gases España S.L.U. (Madrid, Spain) supplied nitrogen gas. Ultrapure water was used and produced by a Milli-Q system (trademark) of Merck Millipore (Billerica, Massachusetts, United States).

### **2.2. Instrumentation and materials**

An Autolab PGSTAT 302N employing GPES software (Metrohm Autolab, Utrecht, Netherlands) equipped with a Frequency Response Analyzer (FRAII) from Eco-Chemie (Utrecht, The Netherlands) was used for Cyclic and Differential Pulse Voltammetric (CV, DPV) measurements and Electrochemical Impedance Spectroscopy (EIS) experiments, respectively. A glassy carbon (GC) electrode of 3 mm diameter was used as the working

electrode whilst the electrochemical cell was completed with a coiled platinum wire and an Ag/AgCl/1 M KCl reference electrode.

The AFM measurements were made with a Nanoscope IIIa system (Veeco, USA) and using silicon FESP cantilevers (Bruker, USA) with a nominal radius of curvature of 8 nm. The topographical and phase-contrast images consisted of 512 x 512 pixels. Kelvin Force Microscopy (KFM) and gradient capacitance (dC/dz) measurements were done with an Agilent 5500 PicoPlus operating in the single pass mode. In these cases, Pt-coated tips (ANSCM-PT from APPNano) with a nominal radius of curvature of 30 nm were used. Note that in KFM, it is measured the contact potential difference (CPD) between the cantilever tip and the sample. This signal is related to the sample work function [42].

## **2.3. Procedures**

### **2.3.1. Synthesis of 2D- MoS<sub>2</sub>**

A top-down solvent exfoliation strategy was used. Briefly, it consisted in first weighting 75 mg of MoS<sub>2</sub> and subsequently adding 10 mL of EtOH/water (45:55, v/v) [43]. Afterwards, the mixture was sonicated for 2 h in a bath, kept at 4 °C for one day, and then centrifuged at 4000 rpm during 45 min. The resulting supernatant was collected and maintained refrigerated while not in use. It is worth to note that we used solvents of non-toxic greenness nature and, from a practical point of view, the low solvents vapour pressure allowed drying the modified electrode at room temperature. As previously reported, working in this way, suspensions of 0.130 mg/mL MoS<sub>2</sub> were obtained according to ICP-MS measurements [22].

### **2.3.2. Synthesis of CB[8]-AuNp**

CB[8]-stabilized gold nanoparticles (CB[8]-AuNp) were synthesized following a previously reported procedure [12,44]. A HAuCl<sub>4</sub> aqueous solution (100 µL, 40 mM) was

added to 40 mL of EtOH/water (1:1 v/v) in an aqua regia-cleaned 100 mL round-bottom flask and homogenised during few seconds to obtain a light-yellow solution. Subsequently, a recently prepared aqueous solution of reductant NaBH<sub>4</sub> (100 µL, 0.1M) was quickly added under energetic hand-swirling to generate the AuNp colloid. This colloid was left undisturbed during one hour and a CB[8] aqueous solution was afterwards added under agitation to achieve a 0.3 mM final concentration. The CB[8]-AuNp were aged during 2 days before use.

### 2.3.3. Synthesis of CB[8]-DNPs

The purchased DNPs solid was first dispersed by sonication in water at a concentration level of 1 mg/mL. Afterwards, a CB[8] quantity was accurately weighted in an eppendorf tube and a defined DNPs dispersion volume was added to achieve a 0.3 mM CB[8] final concentration. This mixture was afterwards subjected to bath sonication to obtain CB[8]-DNPs.

### 2.3.4. Electrochemical sensors preparation

First, the bare GC was polished with alumina powder (0.3 µm), rinsed with ethanol and water under sonication, and dried with N<sub>2</sub>. Next, the modification was performed by successive drop casting of 6 µL of 2D- MoS<sub>2</sub> and 6 µL of CB[8]-AuNp or CB[8]-DNPs suspension, letting to dry at room temperature after each modification step.

### 2.3.5. Atomic Force Microscopic measurements

The topographical measurements were made in the dynamic mode. In all cases, the optical microscope attached to the AFM was used to address the tip to zones where large agglomerates were absent. Different zones were sampled. Likewise, different tips were also used to discard artefacts due to the tip status. Also, several types of samples were studied to be able to better identify the morphological features associated with the different components of the sensor. A similar procedure was followed for the AFM



electrical measurements. These measurements were performed under nitrogen ambient to avoid humidity effects. The analysis of the images was performed using the own software of the equipment as well as with the free-software Gwyddion [45].

#### 2.3.6. Electrochemical Impedance Spectroscopy (EIS) characterization

EIS measurements were carried out in 0.1 M phosphate buffer pH 7.0, employing  $1.0 \cdot 10^{-3}$  M  $MV^{2+}$  as a probe, and at the formal  $MV^{2+}/MV^{+}$  potential. The measurements were performed in a frequency range of 0.1 Hz to 0.1 MHz with a sinusoidal voltage of 5 mV amplitude. All potentials are reported with respect to an Ag/AgCl/1M KCl reference electrode. Either the bare GC electrode or the modified ones (GC/MoS<sub>2</sub> or GC/MoS<sub>2</sub>/CB[8]-DNPs) were employed. The experimental data were presented in the form of Nyquist plots.

#### 2.3.7. Differential Pulse Voltammetry (DPV) measurements

$MV^{2+}$  electrochemical measurements were performed in oxygen-free solutions (using a nitrogen flow) and with the DPV parameters of -0.9 V of initial potential, 60 mV of amplitude, 0.5 s of interval time and 15 mV of potential step (scan rate of 30 mV/s), and 35 s of accumulation time.

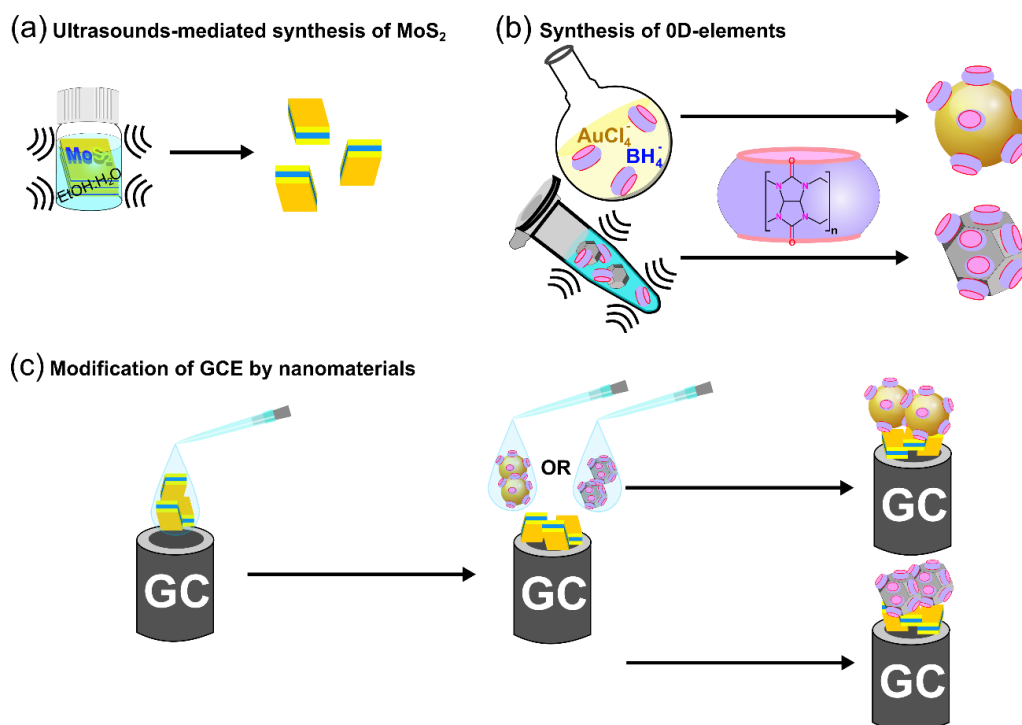
#### 2.3.8. Analysis of $MV^{2+}$ in river water samples.

River water samples were obtained from Záncara River (Camino Dique Mol, Villar de Cañas, Cuenca, Spain) and were kept refrigerated and protected from light until analysis. An aliquot was fortified to  $2.0 \cdot 10^{-5}$  M  $MV^{2+}$ , filtered through 0.45-micron nylon filter,

diluted 1:10 with 0.1 M phosphate buffer pH 7 and, once deoxygenated, subjected to analysis.

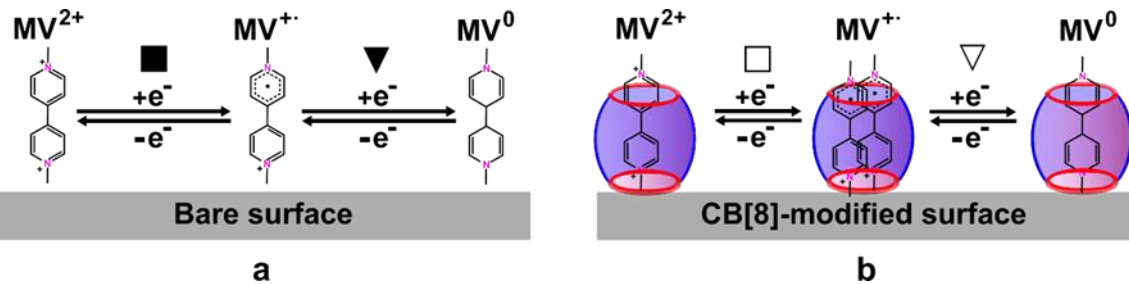
### 3. Results and discussion

In this work, it is evaluated the supramolecular recognition capability of CB[8], when the host is anchored to 0D-materials and forming, together with 2D-MoS<sub>2</sub>, an hybrid system. Scheme 1 summarizes the sensor components and platform construction. The 2D-MoS<sub>2</sub> was first obtained by simple liquid phase exfoliation in EtOH:H<sub>2</sub>O mediated by ultrasounds (Scheme 1a). The 0D-nanomaterials, used along this work, were subjected to CB[n] modification as described in sections 2.3.2 and 2.3.3. The configuration of the as-synthesized suspensions, depicted in Scheme 1b where the CB[n] pumpkin-shaped molecular structure is also shown, are assumed from previous works in literature [5, 6, 12,13,44]. Glassy carbon electrodes were first modified with the 2D-MoS<sub>2</sub> and then with the CB[n]-0D systems as seen in Scheme 1c, constructions that were used to tackle the MV<sup>2+</sup> analysis by voltammetric measurements.



**Scheme 1.** Overview of this work with sensor components and platform construction. (a) 2D-MoS<sub>2</sub> production by a top-down method. (b) 0D-systems modification by CB[n]. (c) Modification of GC electrode: GC/MoS<sub>2</sub>/CB[8]-AuNp and GC/MoS<sub>2</sub>/CB[8]-DNPs sensors construction.

To properly demonstrate the capabilities of our sensor design, it is important to record the response towards MV<sup>2+</sup> with sensors made of each individual nanomaterial employed to assess the need of their combined use as well as the contribution of each separate component on the final response of the dispositive towards the analyte. The electrochemical response of MV<sup>2+</sup> on a GC electrode, either as free analyte or as guest into the CB[7] and CB[8] cavities, is well documented [5,46]. Redox reactions of non-complexed MV<sup>2+</sup> and CB[8]-MV<sup>2+</sup> complex are depicted in scheme 2.



**Scheme 2.** Redox reactions of non-complexed MV<sup>2+</sup> (a) and CB[8]-MV<sup>2+</sup> complex (b). Symbols (■, ▼, □, ▽) correspond to specific waves in Figures 1 and 2.

As shown in Figure 1A-D, the CV response of MV<sup>2+</sup> in an unmodified GC (curves a of each figure, dashed lines) exhibits the expected behaviour described in the literature with waves ascribed to the non-complexed analyte for the MV<sup>2+</sup>/MV<sup>•+</sup> reaction at -0.73 and -0.66 V for the reduction and oxidation, respectively (see also Scheme 2a highlighted with filled squares). The waves at more negative potentials (-1.06 and -1.00 V, featured with filled triangles) are ascribed to MV<sup>•+</sup>/MV<sup>0</sup> system. The adsorptive process associated to

MV<sup>0</sup> previously described [47] is here clearly observed from the feature of the oxidation signal at -1.00 V. Likewise, and according to the literature [5,48,49], the GC-CB[8] electrode (Figure 1A, voltammogram b), discloses new waves due to MV<sup>2+</sup> species hosted by CB[8] (unfilled squares and triangles also seen in Scheme 2b). The waves due to non-complexed MV<sup>2+</sup> species display a much lower intensity than with just the bare electrode. It is worth noting that the CB[8]-accommodated MV<sup>2+</sup>/MV<sup>+</sup> reactions (unfilled squares) take place at less negative potential values (-0.54 and -0.48 V) than in the free guest case (-0.73 and -0.66 V), which is an advantage in terms of selectivity from an electroanalytical perspective. Therefore, this redox pair corresponding to the supramolecular complex will be followed for paraquat analysis. On the contrary, MV<sup>+</sup>/MV<sup>0</sup> reactions arise at -1.35 and -1.11 V (unfilled triangles), that is at more negative potential values than those observed for the non-complexed analyte. Moreover, the inclusion complex formation inhibits the adsorption of MV<sup>0</sup> on the electrode as can be concluded from the decrease of the oxidation wave at -1.00 V.

The 2D-MoS<sub>2</sub>, a well-known nanomaterial with a high surface and semiconducting character, also can prevent the MV<sup>0</sup> adsorption on the electrode, as shown in voltammogram b of Figure 1B, in contrast to the observed MV<sup>+</sup>/MV<sup>0</sup> pair obtained for the bare GC (voltammogram a). Furthermore, the GC/MoS<sub>2</sub> response did not show noticeable peak potential shifts or relevant influence on the peak intensities related to the MV<sup>2+</sup>/MV<sup>+</sup> redox pair. In contrast, intensity improvements of the MV<sup>2+</sup>/MV<sup>+</sup> waves are obtained with the use of DNPs because of their electrocatalysis and large surface contribution (Figure 1C, voltammogram b) [21,43]. It is also noticed that the CB[8] molecular recognition properties remain unaffected when this species is in the hybrid form CB[8]-DNPs (Figure 1C, voltammogram c). A similar conclusion can be extracted from the use of AuNp stabilized with CB[8] depicted in Figure 1D (voltammogram c). In

this figure, the response of a GC modified with commercial AuNp stabilized with citrate (voltammogram b) is also included for comparison. In this later case, no improvement in any of the electrochemical signals can be observed.

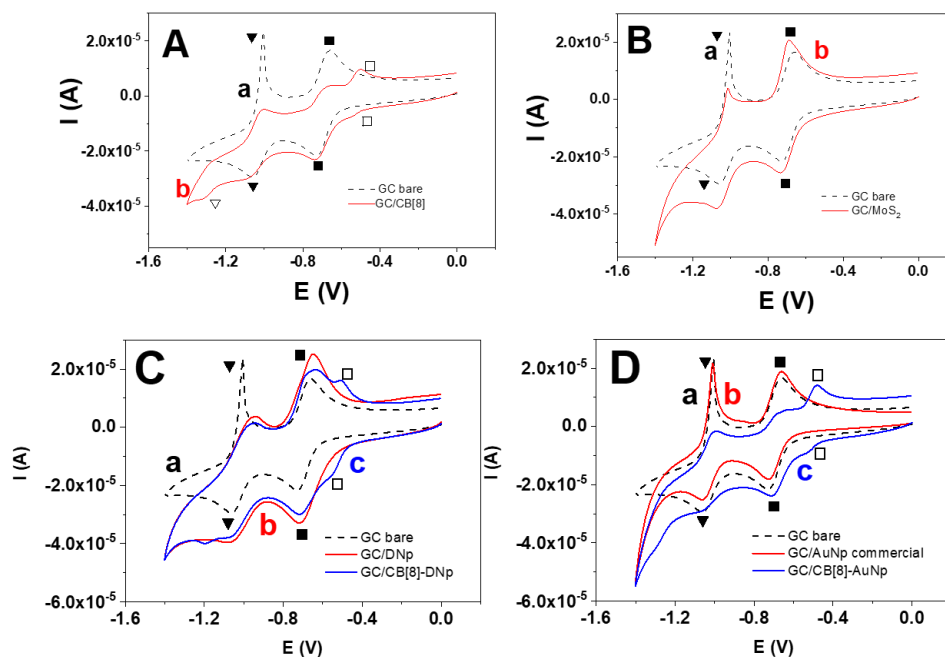


**Figure 1.** Cyclic voltammograms of 1.0 mM  $MV^{2+}$  recorded in 0.1 M phosphate buffer pH 7 at 100 mV/s with a bare GC electrode (curve a, black dashed lines) and electrodes modified with the different nanomaterials under investigation. (A) Effect of CB[8] on the  $MV^{2+}$  response (curve b) studied with the sensor GC/CB[8]. (B) Effect of  $MoS_2$  on the  $MV^{2+}$  response (curve b) with the GC/ $MoS_2$  electrode. (C) Effect of DNPs on  $MV^{2+}$  response, either unmodified (curve b, GC/DNPs) or modified with CB[8] (curve c, GC/CB[8]-DNPs). (D) Effect of AuNp on  $MV^{2+}$  response, either (curve b, GC/AuNp commercial), and of CB[8]-modified AuNp (curve c, GC/CB[8]-AuNp).

From these experiments, it is evident that the CB[8] capability of  $MV^{2+}$  recognition is preserved when the chemical receptor modifies the OD-materials AuNp and DNPs.

Encouraged with these results, we evaluated the performance of hybrids containing the 2D-TMD and the 0D-nanomaterials stabilized with the receptor.

We have previously demonstrated the synergistic effect existing between TMD nanosheets and DNPs towards different electrooxidation processes [22,43,50], like other authors have done with gold nanoparticles [51]. However, the selectivity of these electroanalytical procedures could be improved in order to expand their field of application to more areas including supramolecular recognition. In this sense, we try to contribute to this goal by using CB[n] to achieve an extra selectivity. Therefore, hybrids of MoS<sub>2</sub>/CB[8]-DNPs and MoS<sub>2</sub>/CB[8]-AuNp were employed for the GC electrodes modification. In addition, the same hybrids with CB[7] were studied to know which macrocycle shows the best analytical response since both form supramolecular complexes with MV<sup>2+</sup>, but with different stoichiometry.

As observed in Figure S1, there are no benefits in selectivity by using CB[7] in the hybrid system. Although the electrochemical response of the GC/MoS<sub>2</sub>/CB[7]-AuNp sensor shows increases in currents for all signals, it is not possible to identify that one of analytical interest corresponding to the supramolecular complex. Similar results were obtained with a GC/MoS<sub>2</sub>/CB[7]-DNPs sensor (data not shown). Therefore, the CB[7] homologue was not employed for further investigations, and, in the next step, the response of the whole sensor containing CB[8] is discussed.

As shown in the cyclic voltammograms depicted in Figures 2A and 2B, the electroanalytical signal of the pair of interest, corresponding to the supramolecular complex, is really increased because of the synergistic effect between the nanomaterials employed. The response is clearly higher for the MoS<sub>2</sub>/CB[8]-DNPs combination as it is depicted in Figure 2C that shows the comparison between both systems.

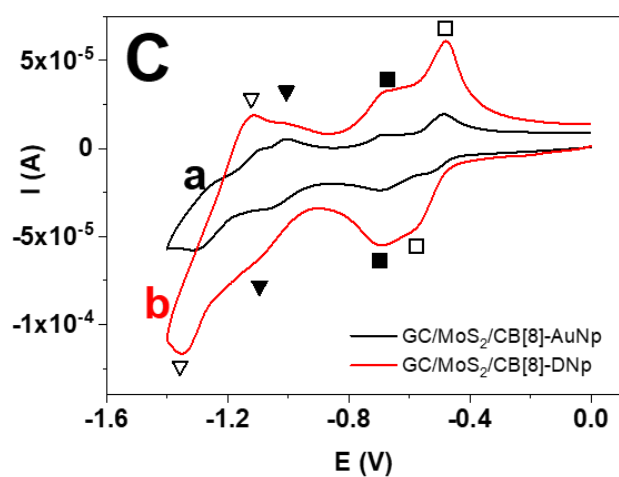
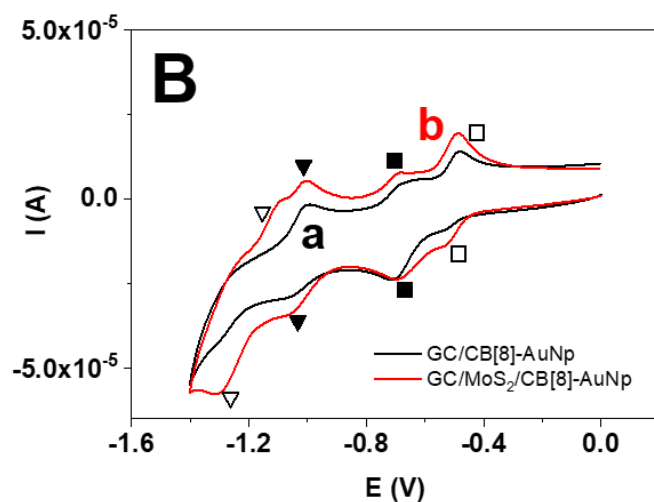
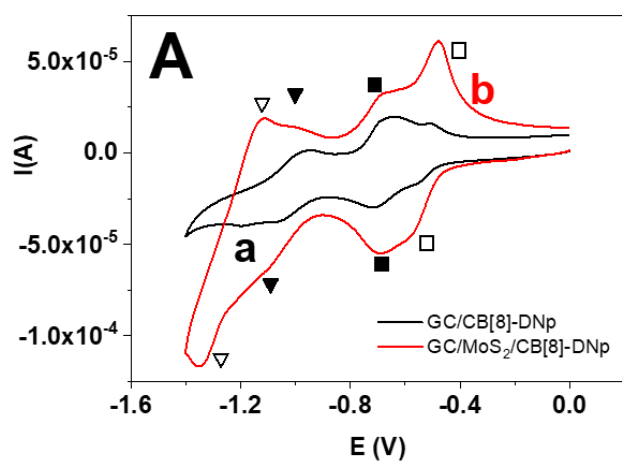


**Figure 2.** Cyclic voltammograms of 1.0 mM  $MV^{2+}$  in 0.1 M phosphate buffer pH 7 at 100 mV/s. (A) (a) GC/CB[8]-DNPs and (b) GC/MoS<sub>2</sub>/CB[8]-DNPs. (B) (a) GC/CB[8]-

AuNp and (b) GC/MoS<sub>2</sub>/CB[8]-AuNp. C) (a) GC/MoS<sub>2</sub>/CB[8]-DNPs and (b) GC/MoS<sub>2</sub>/CB[8]-AuNp.

The synergistic effect of the combination of the three materials is demonstrated by comparing the response of the GC/MoS<sub>2</sub>/CB[8]-DNPs sensor (Figure 2C curve b) with that of sensors containing just MoS<sub>2</sub> (Figure 1B, curve b) and CB[8]-DNPs (Figure 2A, curve a). The most remarkable characteristics are that the peaks of MV<sup>2+</sup>/MV<sup>•+</sup> species inside CB[8] cavity are clearly seen in addition to the peak current increase produced from the nanomaterials combination. This collaborative effect could be due to the certain affinity that CB[8], and to a less extent DNPs, shows to adsorb on the large MoS<sub>2</sub> flake surface as AFM data shows (see below). Thus, more CB[8] molecules on MoS<sub>2</sub> flakes are exposed to MV<sup>2+</sup> molecules.

As a result of all these experiments, and because of the higher intensities obtained when DNPs were used with respect to AuNp, we chose the carbon-based 0D-material for further experimentation related to both: the characterization of the sensor surface (through the evaluation of the electroactive area, AFM and EIS experiments), and the optimization of an analytical method towards MV<sup>2+</sup> analysis.

The electrochemical surface area was determined, with the bare and the different modified electrodes, in a 1M KCl solution containing 10 mM [Ru(NH<sub>3</sub>)<sub>6</sub>]<sup>2+/3+</sup> as redox probe as its electron transfer does not depend on an interaction with a functional group or surface place [52]. The measured peak current (I<sub>p</sub>) is related with the electrochemical surface area (A) through the Randles-Sevick equation:

$$I_p = (2.69 \times 10^5) n^{3/2} A D^{1/2} v^{1/2} C \text{ (equation 1)}$$



where  $v$  is the scan rate,  $n$  the number of electrons,  $D$  the diffusion coefficient ( $9.1 \cdot 10^{-6}$   $\text{cm}^2 \text{ s}^{-1}$  for  $[\text{Ru}(\text{NH}_3)_6]^{2+/3+}$  at  $22^\circ\text{C}$  [53]) and  $C$  the concentration of the redox compound. From the slope of the corresponding  $I_{\text{pa}}$  vs  $v^{1/2}$  plots, electroactive surface areas of  $(0.070 \pm 0.008) \text{ cm}^2$  and  $(0.149 \pm 0.009) \text{ cm}^2$  were obtained for the bare GC and the GC/MoS<sub>2</sub>/CB[8]-DNPs electrodes, respectively. These values confirm that the presence of both nanomaterials results in a considerable increase of the effective area. The redox couple  $\text{MV}^{2+}/\text{MV}^{+}$  encapsulated inside CB[8] showed an analytical interesting displacement to less negative potentials making this system less likely to suffer from potential interferences. Accordingly, the electrochemical oxidation of this pair was the one monitored for the paraquat analysis. Consequently, the scanned potential window was shortened for the optimization of the analytical methodology.

### 3.1. Sensor construction optimization

We optimized the MoS<sub>2</sub> concentration employed in the first layer by using the non-diluted suspension and the ones obtained by dilution in EtOH:H<sub>2</sub>O. A cyclic voltammetry scan of  $\text{MV}^{2+}$  solution was performed with each resulting sensor and the corresponding results are shown in Figure S2A. Since the undiluted TMD suspension (curve b) showed the largest response in comparison with those obtained with the 1:5 and 1:10 dilutions (c and d, respectively), it was chosen for further experimentation. In addition, Figure S2A evinces the above explained MoS<sub>2</sub> effect on the signals enhancement of the  $\text{MV}^{2+}$ -CB[8] complex with respect to the uncomplexed  $\text{MV}^{2+}$  waves (curve a).

In addition, we optimized the CB[8] amount for the sensor GC/MoS<sub>2</sub>/CB[8]-DNPs construction to attain the maximum  $\text{MV}^{2+}$ -CB[8] complex on the surface. Experimentally, three CB[8] concentrations were assayed in the DNPs dispersion. Each aqueous CB[8]-DNPs dispersion was afterwards deposited on a GC/MoS<sub>2</sub> electrode and

1  
2  
3  
4  
5  
6  
7  
8  
9  
10  
11  
12  
13  
14  
15  
16  
17  
18  
19  
20  
21  
22  
23  
24  
25  
26  
27  
28  
29  
30  
31  
32  
33  
34  
35  
36  
37  
38  
39  
40  
41  
42  
43  
44  
45  
46  
47  
48  
49  
50  
51  
52  
53  
54  
55  
56  
57  
58  
59  
60  
61  
62  
63  
64  
65

353 subjected to CV analysis. The corresponding results are depicted in Figure S2B. It is seen  
354 that the larger the CB[8] concentration, the lower the signals due to free  $MV^{2+}$  species,  
355 and the higher the CB[8]- $MV^{2+}$  intensities. However, it should be noted that the 0.6 mM  
356 suspension homogeneity was poorer than the 0.3 mM one, which could result in lower  
357 signals reproducibility. Therefore, 0.3 mM was chosen as optimal for the DNPs  
358 modification.

### 360 ***3.2. AFM and EIS characterization***

361 The sensor surface was characterized by both, AFM and EIS techniques. Figure 3 shows  
362 the characteristic AFM data obtained on the Si/MoS<sub>2</sub> sample. In Figure 3A, a large, 12 x  
363 12  $\mu m^2$ , AFM micrograph is displayed, where large flakes or platelets corresponding to  
364 MoS<sub>2</sub> flakes are clearly visible. In Figure 3B, the surface profile across a single flake,  
365 indicated by the solid line drawn in the AFM image, is shown. The thickness of this flake  
366 is close to 4 nm. A certain roughness is observed on top of the flake. In fact, when the  
367 rms roughness of the flakes of the AFM image is analysed, a value of 1.8 nm is obtained.  
368 This fact can be due to the deposition of tiny structures produced by the preparation  
369 method that are observed in the inset of the Figure 3A that shows, with a greater detail,  
370 the surface of one of these flakes.

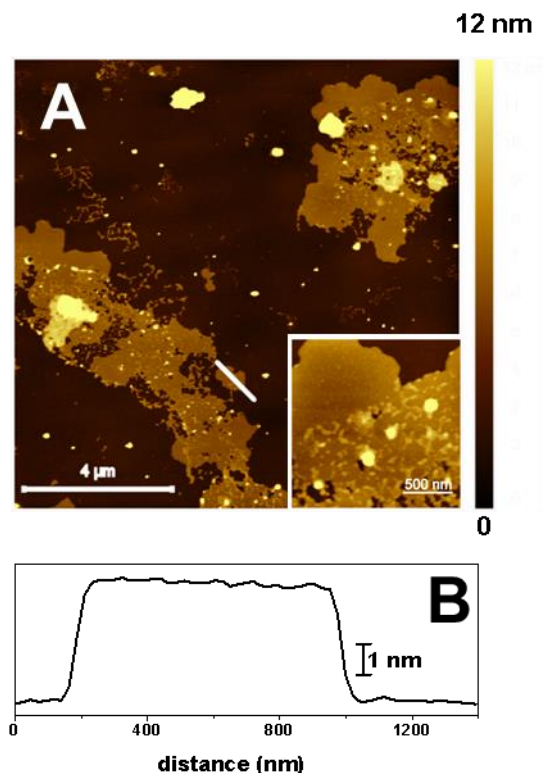


**Figure 3.** (A) 12 x 12  $\mu\text{m}^2$  AFM topographical image of the Si/MoS<sub>2</sub> sample. Inset: 1.7 x 1.7  $\mu\text{m}^2$  AFM image of a MoS<sub>2</sub> flake; (B) Surface profile along the solid line depicted in the top image.

In Figure 4A, it is shown a three-dimensional view of a typical AFM image obtained for the Si/MoS<sub>2</sub>/CB[8]-DNPs sample. Large and rough aggregates of DNPs are formed (notice the large vertical scale). This kind of aggregation of the DNPs particles is well known [43, 54]. We have chosen this sort of 3D representation with illumination in order to evince the thin flakes existing on the surface around the large agglomerates. The top-view image in Figure 4B corresponds to one AFM image taken on one of these flat areas. Here, the flakes structures are clearly observed. In addition, dot structures with different sizes are found scattered on the surface as well as on the flakes. The surface profile along one of the flakes (solid line) is shown in Figure 4E. Now, the flake thickness is close to 6 nm, larger than that of the MoS<sub>2</sub> flakes. Moreover, the flake surface is not as smooth as

that of the MoS<sub>2</sub> flakes. This is better appreciated in the three dimensional view of this flake displayed in Figure 4F. The whole flake surface shows some sort of corrugation, visually different from that observed for the bare MoS<sub>2</sub> flakes (inset of Figure 3A). This corrugation likely comes from CB[8] deposits since its height relative to the flake thickness is always clearly smaller than the average DNPs diameter of 10 nm. Moreover, the thickness of this CB[8] deposit is not constant since, for instance, the bottom part of the flake in Figure 4F (see also Figure 4E) is smoother and thinner than the rest of the flake surface. This fact suggests an uneven CB[8] aggregation on top of the flakes. These differences lead to quite different roughness values for both types of flakes. Thus, whereas the MoS<sub>2</sub> flakes have rms roughness of 1.8 nm, those of the MoS<sub>2</sub>/CB[8]-DNPs sample have a value close to 6 nm. This difference is also seen in the plots of the height distributions of the images (Figure 4G). Both plots display a large peak centred at zero that corresponds to the substrate areas and a second peak, located at higher x-axis values, which corresponds to the flake surface (note that the x-axis represents the pixel height in the image). Clearly, for the MoS<sub>2</sub>/CB[8]-DNPs sample this second peak appears at larger heights (i.e., flake thickness), and also is considerably broader, than the corresponding peak for the bare MoS<sub>2</sub> structures.

In addition to this corrugation, clear dot structures, mainly localized at the perimeter of the flake, are seen in Figure 4F. These well-defined structures, with heights ranging from 8 to 15 nm, should correspond to DNPs. They are also visible in the large top view image (Figure 4B) as the brighter dot structures. They can be found on the flakes as well as on the substrate surface. Their presence on the flake surface also contribute to the long tail of the second peak of the height distribution for the MoS<sub>2</sub>/CB[8]-DNPs sample.

A detailed inspection of the imaged dot structures surrounding the flakes reveals that there are dots of different heights (note that the dot height is not affected by the broader

dimension of the KFM tip). Figure 4H shows the height distribution of these nanostructures. Clearly, there are two peaks, one for the nanostructures with 1-4 nm and other one, broader, for heights in the 10-16 nm. The first one should be related to CB[8] deposits whereas the last one is related to single or aggregated DNPs. This assignment is supported by the KFM and dC/dz images (Figures 4C and D, respectively) taken simultaneously to Figure 4B. The KFM image only shows contrast, with respect to the substrate, at the flakes. In these last structures the CPD is around 0.13 V higher than in the surrounding areas. A close inspection shows that this contrast comes mainly from the thicker zones of the flakes. Note that, in this case, the isolated dots do not yield any contrast. In contrast, Figure 4D shows a dark contrast at the whole flake surface. Furthermore, a darker, although subtle, contrast is found on the dot structures displaying larger heights, i.e. those associated to DNPs, whereas the tiny ones, related to CB[8] isolated deposits do not display any contrast with respect to the substrate. It is not surprising that the imaged structures show different contrast in these two AFM modes since they sample different physical properties. Thus, KFM samples the surface potential whereas the dC/dz signal depends on the local dielectric constant [42]. Finally, it is worth to note that whereas the CB[8] deposits on the substrate are rather small, localized, and isolated, those on top of the flakes are larger in size and more continuous. These data imply that CB[8] presents some sort of affinity for the MoS<sub>2</sub> surface.

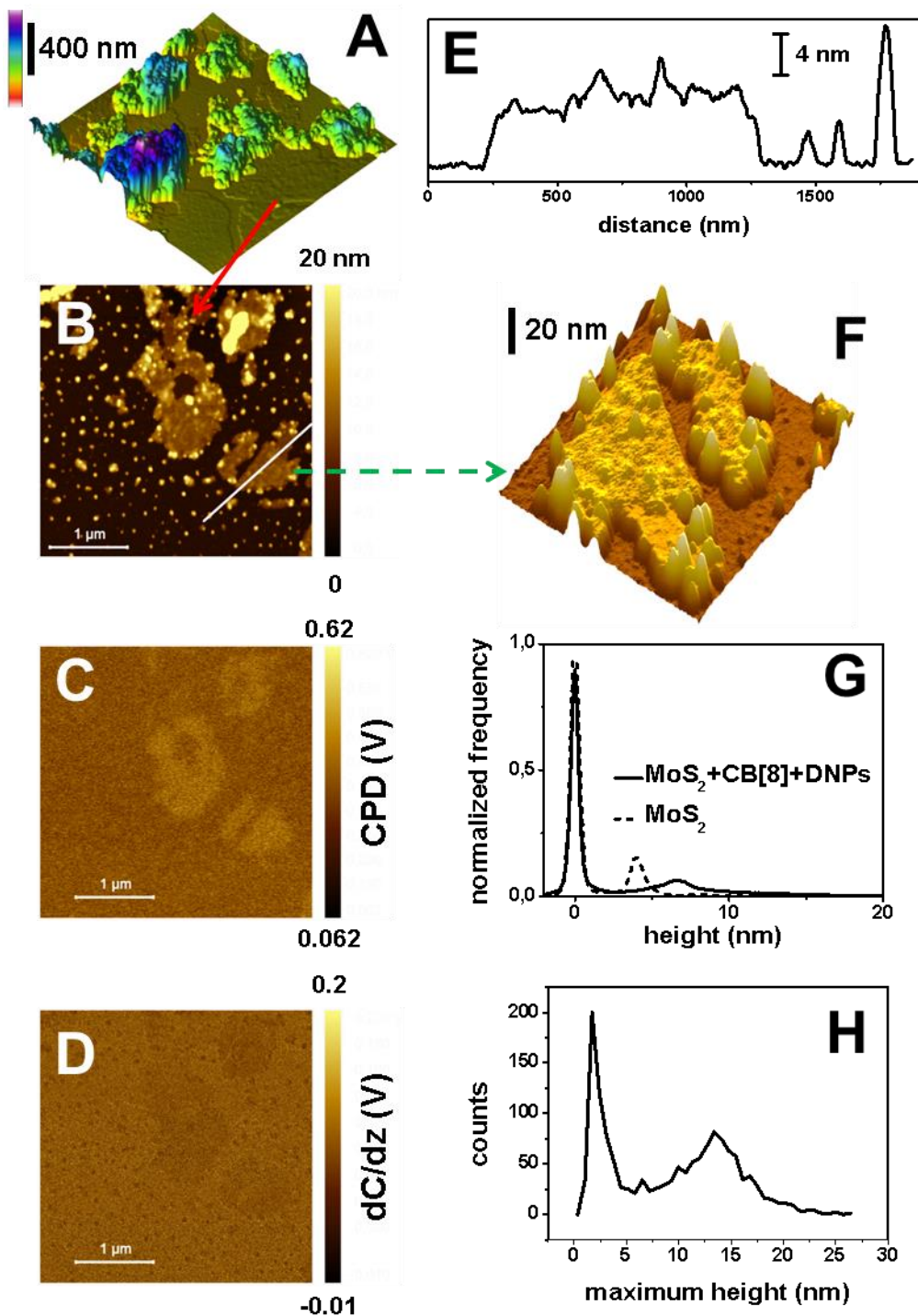


**Figure 4** (A)  $1.2 \times 1.2 \mu\text{m}^2$  3D AFM topographical image of the Si/MoS<sub>2</sub>/CB[8]-DNPs sample. The three-dimensional view is illuminated in order to highlight the MoS<sub>2</sub> flakes on the substrate; (B)  $3.5 \times 3.5 \mu\text{m}^2$  top view AFM image taken on a large flake area similar to that indicated by the solid arrow; (C) Corresponding KFM image; (D) Corresponding

dC/dz image; (E) Surface profile along the solid line depicted in (B). (F)  $1 \times 1.1 \mu\text{m}^2$  3D AFM image of the flake indicated by the dashed arrow; (G) Height distributions for the AFM images shown in Figure 3A ( $\text{MoS}_2$ , dashed line) and (B) ( $\text{MoS}_2/\text{CB}[8]\text{-DNPs}$ , solid line); (H) Distribution of the maximum height of the scattered dot structures surrounding the flakes in (B).

In addition to the AFM morphological characterization, EIS experiments were performed for the characterization of each step of the sensor construction (Figure 5). From the results, we found that the greatest influence of each layer was not in the charge transfer process but rather in the mass-transfer process. The Nyquist plot for the bare GC electrode corresponds to a fast electrochemical process. The recorded slope (slope  $\approx 1$ ) in the region of the low frequencies suggests that semi-infinite linear diffusion rules the mass-transfer process [55]. However, when the modified electrodes are investigated, slopes higher than 1, related to adsorption processes (1.4 and 1.7 for GC/ $\text{MoS}_2$  and GC/ $\text{MoS}_2/\text{CB}[8]\text{-DNPs}$ , respectively) are observed [56].

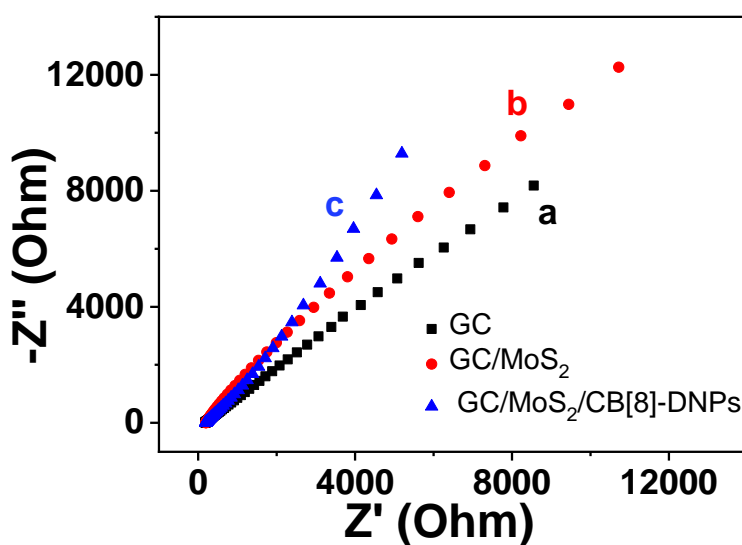


**Figure 5.** Nyquist plots of 1.0 mM  $MV^{2+}$  solutions in phosphate buffer 0.1 M at the formal potential of the redox pair, in the 0.1 Hz to 0.1 MHz frequency range. Sinusoidal voltage of 5 mV amplitude.

### 3.3. Instrumental variables optimization

Differential pulse voltammetry (DPV) offers a greater sensitivity than CV, which is required for analytical purposes. Accordingly, we moved to DPV, being the parameters of amplitude, scan rate (studied by means of both interval time and potential step) firstly scrutinized. An amplitude range of 10 to 100 mV in steps of 10 mV was assayed. The best result was obtained for 60 mV in a compromise between sensitivity and selectivity because, the higher the amplitude, the greater the current intensity but also the broader the peak.

Next, we optimized the scan rate through the individual variation of the interval time and the potential step. The best results, in terms of the peak current, are obtained for an interval time and a potential step of 0.5 s and 15 mV, respectively. These conditions lead to a scan rate of 30 mV/s.

Moreover, we tested the effect of the accumulation time at the initial potential (-0.9 V) in the analytical signal. This variable was explored at three  $MV^{2+}$  levels, specifically 2.5, 5.0 and 7.5  $\mu$ M, and the results are presented in Figure S3. We found that the higher the accumulation time, the greater the recorded peak intensity with larger currents for higher concentrations. At the concentration of  $7.5 \times 10^{-6}$  M an increased intensity was observed during the first 20 seconds. This was not the case at  $5.0 \times 10^{-6}$  M where the GC/MoS<sub>2</sub>/CB[8]-DNPs surface was saturated for times longer than 25 s. At  $2.5 \times 10^{-6}$  M a similar behaviour was observed but now the plateau was reached at 35 s. Therefore, this value was chosen as the optimum to be capable of achieving the  $MV^{2+}$  quantification at low concentration levels.



### 3.4. Influence of the $MV^{2+}$ concentration in the peak current. Analytical data.

Once the sensor construction and the experimental variables were optimized, we studied the influence of the  $MV^{2+}$  concentration in the peak current. The corresponding results are depicted in Figure 6.

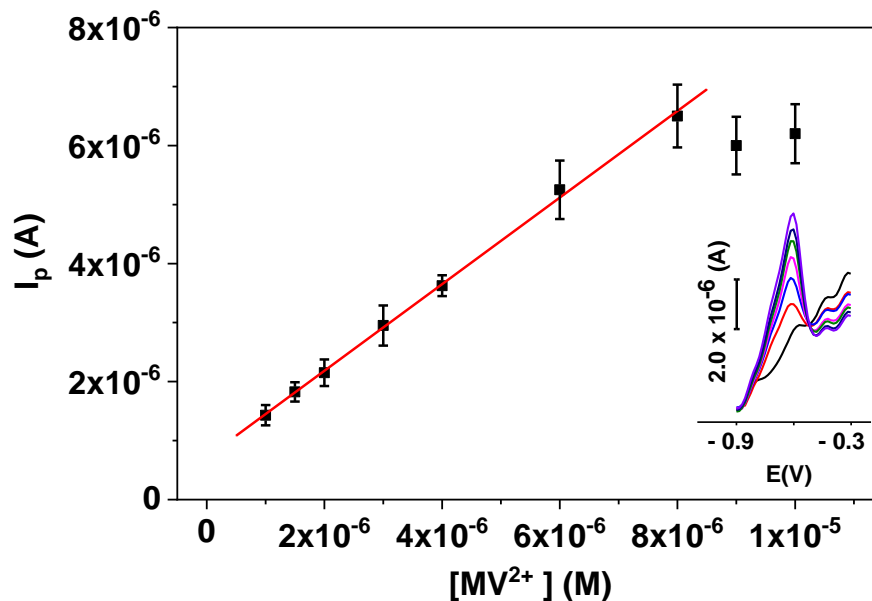


**Figure 6.** DPV calibration graph of  $MV^{2+}$  with GC/MoS<sub>2</sub>/CB[8]-DNPs in 0.1 M phosphate buffer pH 7. Accumulation time = 35 s,  $E_{ac}$  = -0.9 V, amplitude = 60 mV, scan rate = 30 mV/s.

The voltammograms in the inset show the signals of supporting electrolyte (black line) and for  $1.0 \cdot 10^{-6}$  to  $8.0 \cdot 10^{-6}$  M  $MV^{2+}$  where it is seen that the higher the analyte concentration, the greater the intensity of the peak corresponding to the supramolecular complex. The corresponding calibration plot shows averaged peak currents and standard deviations ( $n=3$ ) for each assayed concentration. Signals and concentrations were linearly correlated by the equation  $I_p$  (A) =  $(0.73 \pm 0.01)$   $[MV^{2+}]$  (M) +  $(0.72 \pm 0.05) \cdot 10^{-6}$  with

$R^2 = 0.998$  in the concentration range of  $(0.73 - 8.0) \times 10^{-6}$  M. For all the concentration levels inspected, the relative standard deviations ( $n=3$ ) were lower than 11% and 3.6% for different sensors and in terms of repeatability in successive cycles, respectively. The good fit between the experimental data and the fitted equation is demonstrated by  $E_r$  values lower than 3.0%. The limit of detection (LD) and the limit of quantification (LQ) were calculated from the standard deviation of blank solution data and  $2.2 \cdot 10^{-7}$  M and  $7.3 \cdot 10^{-7}$  M were found, respectively. This limit of quantification is below the Drinking Water Equivalent Level (DWEL) of the United States Environmental Protection Agency for paraquat [57]. For comparative purposes, Table 1 summarizes the analytical properties of several sensors for  $MV^{2+}$  analysis found in the literature. The detection limit values herein included are similar to [39], or even better than [38], those reported with different electrochemical sensors. Although other methods [28,32] report lower detection limits with similar linear ranges for quantification purposes, it is worth noting that they lack the selectivity improvement derived from the CB[8] molecular recognition properties.

**Table 1.** Comparative analytical data of electrochemical sensors for  $MV^{2+}$  analysis

Sensing surface	LD ( $\mu M$ )	Linear range ( $\mu M$ )	Reference
(BiFE)/Cu	0.093	0.66 - 48	[28]
HAP-CPE	0.015	0.8 - 20	[32]
DNA/AuNp/Au	1.3	5.6 - 1000	[38]
(Cu <sub>2</sub> O/PVP-GNs/GC-RDE)	0.27	1 - 200	[39]
Au ultramicroelectrode	0.12	1 - 10	[40]
PHTH-based PY GE	0.1	0.5 - 29.1	[41]
GC/MoS <sub>2</sub> /CB[8]-DNPs	0.22	0.73 - 8.0	This work

(BiFE)/Cu: ex situ bismuth-film electrode. HAP-CPE: hydroxyapatite-modified carbon paste electrode. DNA/AuNp/Au: DNA/gold nanoparticles modified gold electrode. Cu<sub>2</sub>O/PVP-GNs/GC-RDE: Cu<sub>2</sub>O/polyvinyl pyrrolidone-graphene modified glassy carbon-rotating disk electrode. PHTH-based PY GE: Phthalocyanine-based pyrolytic graphite electrode

### 3.5. Interference studies

It has been previously demonstrated that the use of CB[8] allows to eliminate the interference of: i) analytes negatively charged, ii) analytes that do not fit with the cavity size, iii) substances that could be detected at more negative potentials than  $-0.54$  V because of having included CB8 in the sensor design. To evaluate the selectivity of our sensor, we tested different possible interference compounds that could be present together with  $MV^{2+}$  in aqueous samples: the fungicides thiabendazole (Tbz) and carbendazim (Cbz), and the aromatic diamine 4,4'-oxydianiline (Oxy). The experiments were performed as follows: solutions containing  $MV^{2+}$  at a concentration level of  $8.0 \cdot 10^{-6}$  M  $MV^{2+}$  were measured alone and mixed with increasing concentrations of the corresponding interference. It was considered that a compound causes interference at a concentration level that produces a variation of 10 % in the initial  $MV^{2+}$  intensity current. From the obtained results, no interference was found for any of the fungicides up to 1:1 concentration ratio respect to  $MV^{2+}$ . Moreover, increasing concentrations of Oxy did not produce interference up to  $4.0 \cdot 10^{-5}$  M, which represents a 5-fold concentration level respect to  $MV^{2+}$ .

### 3.6. Analytical application

$MV^{2+}$  presents a high water solubility and its half-life in the environment is relatively large. Therefore, the performance of the developed GC/MoS<sub>2</sub>/CB[8]-DNPs sensor was tested towards the  $MV^{2+}$  analysis in river water samples from Zánacara river (Spain). To this end, river water aliquots of 1.0 mL, unfortified and fortified at different  $MV^{2+}$  concentrations, were diluted to 10.0 mL, with 0.1 M phosphate buffer pH 7 employed as electrolyte. Although the DPV response recorded from the fortified solutions showed a linear increase of the current with increasing  $MV^{2+}$  amounts, no  $MV^{2+}$  was detected in the unfortified sample. Therefore, an aliquot of the river water was fortified at a  $2.0 \cdot 10^{-}$

<sup>5</sup> M level, just subjected to a filtration pretreatment, diluted 1:10 with the electrolyte and subjected to DPV analysis by the standard addition procedure. Figure S4 shows the voltammograms recorded in this complex sample matrix where the MV<sup>2+</sup> signal (red line) is clearly observed with respect to the electrolyte. Figure S4 also shows the averaged peak currents of the MV<sup>2+</sup> standard additions in the  $1.0 \cdot 10^{-6}$  to  $5.0 \cdot 10^{-6}$  M range. The peak current fitted linearly with the analyte added according to the equation:  $I_p (A) = (1.0 \pm 0.1) [MV^{2+}] (M) + (2.1 \pm 0.2) \cdot 10^{-6}$  with  $r = 0.990$  ( $n=3$ ). Data analysis was afterwards made to assess whether the standard addition method was necessary or a simpler interpolation in the external calibration equation could be used. We found significant differences between the slopes of both calibration procedures, namely  $(0.73 \pm 0.01)$  by the external calibration procedure and  $(1.0 \pm 0.1)$  by the standard addition methodology, as the calculated t value was 4.9 while the tabulated t (95%) value was 2.8. These results led us to conclude that matrix interference is produced and, consequently, standard addition is required for MV<sup>2+</sup> quantification. A concentration of  $(2.0 \pm 0.1) \cdot 10^{-5}$  M was found which means a good 100% of recovery with an enough precision (6.4 % RSD) calculated from three different analyses.

#### 4. Conclusions

We present the combination of materials with different dimensionality in the design of an electrochemical sensor, namely GC/MoS<sub>2</sub>/CB[8]-DNPs. The sensor design combines the benefits in sensitivity derived from the use of MoS<sub>2</sub> nanosheets and diamond nanoparticles together with the selectivity derived from the molecular recognition properties of CB[8], which are evidenced towards the determination of the pesticide paraquat. In addition, we have demonstrated that the molecular receptor CB[8] retains its recognition properties when functionalising either gold or diamond nanoparticles. AFM

characterization shows and enhanced adsorption on the MoS<sub>2</sub> flake surface of CB[8] and to a less extent of DNPs. In addition, KFM measurements allow to distinguish between CB[8] and DNP deposits. In the best of our knowledge, neither CB[n]-modified DNPs nor the use of these macrocycles and 2D-TMD in the same device had ever been explored before. Comparing both functionalized nanoparticles, AuNp and DNPs, the excellent electrocatalytic properties of diamond ones, make the combination CB[8]-DNPs a promising functionalized material for different electroanalytical applications. The sensor responds linearly to MV<sup>2+</sup> from 0.73 · 10<sup>-6</sup> to 8.0 · 10<sup>-6</sup> M with a LD of 2.2 · 10<sup>-7</sup> M. Moreover, the sensor capability to determine MV<sup>2+</sup> in real river samples has been proved with excellent recoveries for fortified samples at the μM level.

**Funding:** The authors acknowledge financial support from the Spanish MINECO (MAT2017-85089-C2-1-R, MAT2017-85089-C2-2-R, PID2020-113142RB-C22) and the Comunidad Autónoma de Madrid (P2018/NMT-4349, TRANSNANOAVANSENS-CM).

## References

- [1] H. Luo, L.-X. Chen, Q.-M. Ge, M. Liu, Z. Tao, Y.-H. Zhou, H. Cong, Applications of macrocyclic compounds for electrochemical sensors to improve selectivity and sensitivity, *J. Incl. Phenom. Macrocycl. Chem.* 95 (2019) 171–198.
- [2] S.J. Barrow, S. Kasera, M.J. Rowland, J. del Barrio, O.A. Scherman, Cucurbituril-Based Molecular Recognition, *Chem. Rev.* 115 (2015) 12320–12406.
- [3] H. Cong, Z.-J. Li, Q.-X. Geng, Z. Tao, G. Wei, Modification of carbon paste electrode with cucurbit[8]uril and its recognition to phenols, *J. Incl. Phenom. Macrocycl. Chem.* 81 (2015) 493–498.
- [4] M. del Pozo, J. Mejías, P. Hernández, C. Quintana, Cucurbit[8]uril-based

electrochemical sensors as detectors in flow injection analysis. Application to  
dopamine determination in serum samples, *Sens. Actuators, B* 193 (2014) 62–  
69.

[5] M. Buaki-Sogo, M. Del Pozo, P. Hernández, H. García, C. Quintana, Graphene in  
combination with cucurbit[n]urils as electrode modifiers for electroanalytical  
biomolecules sensing, *Talanta*. 101 (2012) 135–140.

[6] L. Shao, J. Zhong, Y. Ren, H. Tang, X. Wang, Perhydroxy-CB[6] decorated  
graphene oxide composite for uranium(VI) removal, *J. Radioanal. Nucl. Chem.*  
311 (2017) 627–635.

[7] R.D. Tandel, J. Seetharamappa, Porous Reduced Graphene Oxide beta-  
cyclodextrin Modified Electrode as Enhanced Sensing Platform for the  
Determination of Dihydrochalcone: Phloretin, *J. Electrochem. Soc.* 165 (2018)  
H629-H637.

[8] A.G. dos Santos Neto, C.S. de Sousa, A. da S. Freires, S.M. Silva, H. Zanin, F.S.  
Damos, R. de C. Silva Luz, Electrochemical sensor for detection of imipramine  
antidepressant at low potential based on oxidized carbon nanotubes,  
ferrocenecarboxylic acid, and cyclodextrin: application in psychotropic drugs and  
urine samples, *J. Solid State Electrochem.* 22 (2018) 1385–1394.

[9] H. Huang, M. Liu, R. Jiang, J. Chen, L. Mao, Y. Wen, J. Tian, N. Zhou, X. Zhang,  
Y. Wei, Facile modification of nanodiamonds with hyperbranched polymers based  
on supramolecular chemistry and their potential for drug delivery, *J. Colloid  
Interface Sci.* 513 (2018) 198–204.

[10] G. Cavallaro, G. Lazzara, E. Rozhina, S. Konnova, M. Kryuchkova, N.  
Khaertdinov, R. Fakhrullin, Organic-nanoclay composite materials as removal  
agents for environmental decontamination, *Rsc Adv.* 9 (2019) 40553–40564.

- [11] L. Qi, R. Wang, H.-Z. Yu, Electrochemical Quantitation of Supramolecular  
Excipient@Drug Complexation: A General Assay Strategy Based on Competitive  
Host Binding with Surface-Immobilized Redox Guest, *Anal. Chem.* 92 (2020)  
2168–2175.
- [12] M. del Pozo, E. Blanco, P. Hernández, J.A. Casas, C. Quintana, Catalytic  
efficiency of macrocyclic-capped gold nanoparticles: cucurbit[n]urils versus  
cyclodextrins, *J. Nanoparticle Res.* 20 (2018) 121.
- [13] P. Xu, Q. Feng, X. Yang, S. Liu, C. Xu, L. Huang, M. Chen, F. Liang, Y. Cheng,  
Near Infrared Light Triggered Cucurbit[7]uril-Stabilized Gold Nanostars as a  
Supramolecular Nanoplatfrom for Combination Treatment of Cancer,  
*Bioconjugate Chem.* 29 (2018) 2855–2866.
- [14] H. Li, X. Hu, J. Zhao, K. Koh, H. Chen, A label-free impedimetric sensor for the  
detection of an amphetamine-type derivative based on cucurbit[7]uril-mediated  
three-dimensional AuNPs, *Electrochem. Commun.* 100 (2019) 126-133.
- [15] M. del Pozo, E. Casero, C. Quintana, Visual and spectrophotometric determination  
of cadaverine based on the use of gold nanoparticles capped with cucurbiturils or  
cyclodextrins, *Microchim. Acta.* 184 (2017) 2107–2114.
- [16] Y. Hao, L.-C. Xu, J. Pu, L. Wang, L.-F. Huang, Stable zigzag edges of transition-  
metal dichalcogenides with high catalytic activity for oxygen reduction,  
*Electrochim. Acta* 338 (2020) 135865.
- [17] X. Wang, Y. Zhang, H. Si, Q. Zhang, J. Wu, L. Gao, X. Wei, Y. Sun, Q. Liao, Z.  
Zhang, K. Ammarah, L. Gu, Z. Kang, Y. Zhang, Single-Atom Vacancy Defect to  
Trigger High-Efficiency Hydrogen Evolution of MoS<sub>2</sub>, *J. Am. Chem. Soc.* 142  
(2020) 4298–4308.
- [18] E. Lorchat, L.E.P. López, C. Robert, D. Lagarde, G. Froehlicher, T. Taniguchi, K.

- Watanabe, X. Marie, S. Berciaud, Filtering the photoluminescence spectra of atomically thin semiconductors with graphene, *Nat. Nanotechnol.* 15 (2020) 283–288.
- [19] M. del Pozo, C. Sánchez-Sánchez, L. Vázquez, E. Blanco, M. Dolores Petit-Domínguez, J.A. Martín-Gago, E. Casero, C. Quintana, Differential pulse voltammetric determination of the carcinogenic diamine 4,4'-oxydianiline by electrochemical preconcentration on a MoS<sub>2</sub> based sensor, *Microchim. Acta* 186 (2019) 793.
- [20] A. V. Shvidchenko, E.D. Eidelman, A.Y. Vul', N.M. Kuznetsov, D.Y. Stolyarova, S.I. Belousov, S.N. Chvalun, Colloids of detonation nanodiamond particles for advanced applications, *Adv. Colloid Interface Sci.* 268 (2019) 64–81.
- [21] N. Yang, S. Yu, J. V. MacPherson, Y. Einaga, H. Zhao, G. Zhao, G.M. Swain, X. Jiang, Conductive diamond: Synthesis, properties, and electrochemical applications, *Chem. Soc. Rev.* 48 (2019) 157–204.
- [22] E. Blanco, L. Hristova, R. Martínez-Moro, L. Vázquez, G.J. Ellis, L. Sánchez, M. del Pozo, M.D. Petit-Domínguez, E. Casero, C. Quintana, A 2D tungsten disulphide/diamond nanoparticles hybrid for an electrochemical sensor development towards the simultaneous determination of sunset yellow and quinoline yellow, *Sens. Actuators, B* 324 (2020) 128731.
- [23] S. Chowdhury, Y. Nassar, L. Guy, D. Frath, F. Chevallier, E. Dumont, A.P. Ramos, G.J.-F. Demets, C. Bucher, Photo/redox-responsive 2D-Supramolecular assembly involving Cucurbit[8]uril and a star-shaped porphyrin tecton, *Electrochim. Acta* 316 (2019) 79–92.
- [24] S. Datta, M.L. Saha, N. Lahiri, G. Yu, J. Louie, P.J. Stang, Hierarchical Self-Assembly of a Water-Soluble Organoplatinum(II) Metallacycle into Well-Defined



- 663 Nanostructures, *Org. Lett.* 20 (2018) 7020–7023.
- 664 [25] S. Sinn, F. Biedermann, Chemical Sensors Based on Cucurbit[n]uril Macrocycles,  
665 *Isr. J. Chem.* 58 (2018) 357–412.
- 666 [26] Y. Huang, H. Zhan, P. Bhatt, S. Chen, Paraquat Degradation From Contaminated  
667 Environments: Current Achievements and Perspectives, *Front. Microbiol.* 10  
668 (2019) 1754.
- 669 [27] Y. Li, L. Liu, H. Kuang, C. Xu, Preparing monoclonal antibodies and developing  
670 immunochromatographic strips for paraquat determination in water, *Food Chem.*  
671 311 (2020) 125897.
- 672 [28] L.C.S. de Figueiredo-Filho, V.B. dos Santos, B.C. Janegitz, T.B. Guerreiro, O.  
673 Fatibello-Filho, R.C. Faria, L.H. Marcolino-Junior, Differential Pulse  
674 Voltammetric Determination of Paraquat Using a Bismuth-Film Electrode,  
675 *Electroanalysis*. 22 (2010) 1260–1266.
- 676 [29] W.-T. Tsai, Status of herbicide use, regulatory management and case study of  
677 paraquat in Taiwan, *Environ. Dev. Sustain.* 22 (2020) 2673–2683.
- 678 [30] J. Antonio Buendia, G.J. Restrepo Chavarriaga, A.F. Zuluaga, Burden of paraquat  
679 poisoning in the department of Antioquia, Colombia, *Bmc Pharmacol. Toxicol.* 20  
680 (2019) 11.
- 681 [31] S.H. Zyoud, Investigating global trends in paraquat intoxication research from  
682 1962 to 2015 using bibliometric analysis, *Am. J. Ind. Med.* 61 (2018) 462–470.
- 683 [32] M.A. El Mhanunedi, M. Bakasse, A. Chtaini, Square-wave voltammetric  
684 determination of paraquat at carbon paste electrode modified with hydroxyapatite,  
685 *Electroanalysis* 19 (2007) 1727–1733.
- 686 [33] T. Fernandes, S.F. Soares, T. Trindade, A.L. Daniel-da-Silva, Magnetic Hybrid

- 687 Nanosorbents for the Uptake of Paraquat from Water, *Nanomaterials* 7 (2017) 68.
- 688 [34] Y. Nagatomi, T. Yoshioka, M. Yanagisawa, A. Uyama, N. Mochizuki, Rapid  
689 analysis of paraquat and diquat in beer and malt using LC-MS/MS, *J. Pestic. Sci.*  
690 38 (2013) 144–146.
- 691 [35] F. Du, L. Sun, Q. Zen, W. Tan, Z. Cheng, G. Ruan, J. Li, A highly sensitive and  
692 selective “on-off-on” fluorescent sensor based on nitrogen doped graphene  
693 quantum dots for the detection of  $\text{Hg}^{2+}$  and paraquat, *Sens. Actuators, B* 288 (2019)  
694 96–103.
- 695 [36] N. Kishikawa, S. Higuchi, K. Ohya, K. Nakashima, N. Kuroda, A simple and  
696 rapid chemiluminescence assay for on-site analysis of paraquat using a portable  
697 luminometer, *Forensic Toxicol.* 31 (2013) 301–306.
- 698 [37] A.M. Pathan, M.A. Baseer, A.B. Kadam, S.B. Junne, A Novel Chromogenic Spray  
699 Reagent for Thin-Layer Chromatographic Analysis of Paraquat and Design of an  
700 Ultra-Low-Cost Sensor for On-The-Field Detection of Viologens, *J. Planar*  
701 *Chromatogr.-Mod. TLC* 32 (2019) 335–338.
- 702 [38] J.A. Ribeiro, C.A. Carreira, H.J. Lee, F. Silva, A. Martins, C.M. Pereira,  
703 Voltammetric determination of paraquat at DNA-gold nanoparticle composite  
704 electrodes, *Electrochim. Acta* 55 (2010) 7892–7896.
- 705 [39] X. Ye, Y. Gu, C. Wang, Fabrication of the  $\text{Cu}_2\text{O}$ /polyvinyl pyrrolidone-graphene  
706 modified glassy carbon-rotating disk electrode and its application for sensitive  
707 detection of herbicide paraquat, *Sens. Actuators, B* 173 (2012) 530–539.
- 708 [40] O.B. da Silva, S.A.S. Machado, Evaluation of the detection and quantification  
709 limits in electroanalysis using two popular methods: application in the case study  
710 of paraquat determination, *Anal. Methods* 4 (2012) 2348–2354.
- 711 [41] I.C. Lopes, D. De Souza, S.A.S. Machado, A.A. Tanaka, Voltammetric detection

of paraquat pesticide on a phthalocyanine-based pyrolytic graphite electrode, *Anal. Bioanal. Chem.* 388 (2007) 1907–1914.

[42] M.J. Cadena, R. Misiego, K.C. Smith, A. Avila, B. Pipes, R. Reifemberger, A. Raman, Sub-surface imaging of carbon nanotube-polymer composites using dynamic AFM methods, *Nanotechnology* 24 (2013) 135706.

[43] M.D. Petit- Domínguez, C. Quintana, L. Vázquez, M. del Pozo, I. Cuadrado, A.M. Parra-Alfambra, E. Casero, Synergistic effect of MoS<sub>2</sub> and diamond nanoparticles in electrochemical sensors: determination of the anticonvulsant drug valproic acid, *Microchim. Acta* 185 (2018) 334.

[44] T.-C.Lee, O.A. Scherman, A Facile Synthesis of Dynamic Supramolecular Aggregates of Cucurbit[n]uril (n=5-8) Capped with Gold Nanoparticles in Aqueous Media, *Chem. - Eur. J.* 18 (2012) 1628–1633.

[45] D. Nečas, P. Klapetek, Gwyddion: An open-source software for SPM data analysis, *Cent. Eur. J. Phys.* 10 (2012) 181–188.

[46] Y. Ling, J.T. Mague, A.E. Kaifer, Inclusion complexation of diquat and paraquat by the hosts cucurbit[7]uril and cucurbit[8]uril, *Chem. - Eur. J.* 13 (2007) 7908–7914.

[47] L. Xiao, G.G. Wildgoose, R.G. Compton, Investigating the voltammetric reduction of methylviologen at gold and carbon based electrode materials. Evidence for a surface bound adsorption mechanism leading to electrode ‘protection’ using multi-walled carbon nanotubes, *New J. Chem.* 32 (2008) 1628–1633.

[48] A.E. Kaifer, W. Li, S. Yi, Cucurbiturils as Versatile Receptors for Redox Active Substrates, *Isr. J. Chem.* 51 (2011) 496–505.

[49] M. del Pozo, E. Blanco, E. Fatás, P. Hernández, C. Quintana, New supramolecular interactions for electrochemical sensors development: different cucurbit[8]uril

737 sensing platform designs, *Analyst* 137 (2012) 4302–4308.

738 [50] E. Blanco, L. Arias, L. Vázquez, M. del Pozo, L. Sánchez, M.D. Petit-Domínguez,  
739 C. Quintana, E. Casero, Sensor based on diamond nanoparticles and WS<sub>2</sub> for  
740 ponceau 4R and tartrazine determination: Influence of green solvents employed for  
741 WS<sub>2</sub> exfoliation, *FlatChem* 23 (2020) 100185.

742 [51] A.T.E. Vilian, B. Dinesh, S.-M. Kang, U.M. Krishnan, Y.S. Huh, Y.-K. Han,  
743 Recent advances in molybdenum disulfide-based electrode materials for  
744 electroanalytical applications, *Microchim. Acta* 186 (2019) 203.

745 [52] P. Chen, R.L. McCreery, Control of Electron Transfer Kinetics at Glassy Carbon  
746 Electrodes by Specific Surface Modification, *Anal. Chem.* 68 (1996) 3958–3965.

747 [53] C. Beriet, D. Pletcher, A further microelectrode study of the influence of  
748 electrolyte concentration on the kinetics of redox couples, *J. Electroanal. Chem.*  
749 375 (1994) 213–218.

750 [54] A. Krüger, F. Kataoka, M. Ozawa, T. Fujino, Y. Suzuki, A.E. Aleksenskii, A.Y.  
751 Vul', E. Osawa, Unusually tight aggregation in detonation nanodiamond:  
752 Identification and disintegration, *Carbon* 43 (2005) 1722–1730.

753 [55] M. Sluyters-Rehbach, J.H. Sluyters, *Electroanalytical Chemistry*, Marcel Dekker  
754 Inc., New York, 1970.

755 [56] E. Fatás-Lahoz, M. Sluyters-Rehbach, J.H. Sluyters, The investigation of the  
756 adsorptive behaviour of electroactive species by means of admittance analysis: Part  
757 II. Anion-induced adsorption of cadmium(II) from bromide and iodide solutions at  
758 the dropping mercury electrode, *J. Electroanal. Chem. Interfacial Electrochem.* 136  
759 (1982) 59–81.

760 [57] U.S.E.P. Agency, O. Water, 2018 Edition of the Drinking Water Standards and  
761 Health Advisories Tables.

## Supplementary Information

### **A supramolecular hybrid sensor based on cucurbit[8]uril, 2D-molibdenum disulphide and diamond nanoparticles towards methyl viologen analysis.**

Elías Blanco<sup>a</sup>, Laura Rocha<sup>a</sup>, María del Pozo<sup>a</sup>, Luis Vázquez<sup>b</sup>, María Dolores Petit-Domínguez<sup>a</sup>, Elena Casero<sup>a</sup>, Carmen Quintana<sup>a\*</sup>

<sup>a</sup>Departamento de Química Analítica y Análisis Instrumental. Facultad de Ciencias. c/ Francisco Tomás y Valiente, N°7. Campus de Excelencia de la Universidad Autónoma de Madrid. 28049 Madrid. Spain.

<sup>b</sup>ESISNA group, Instituto de Ciencia de Materiales de Madrid (CSIC). c/ Sor Juana Inés de la Cruz N°3. Campus de Excelencia de la Universidad Autónoma de Madrid. 28049 Madrid. Spain

\*Corresponding author email: carmen.quintana@uam.es

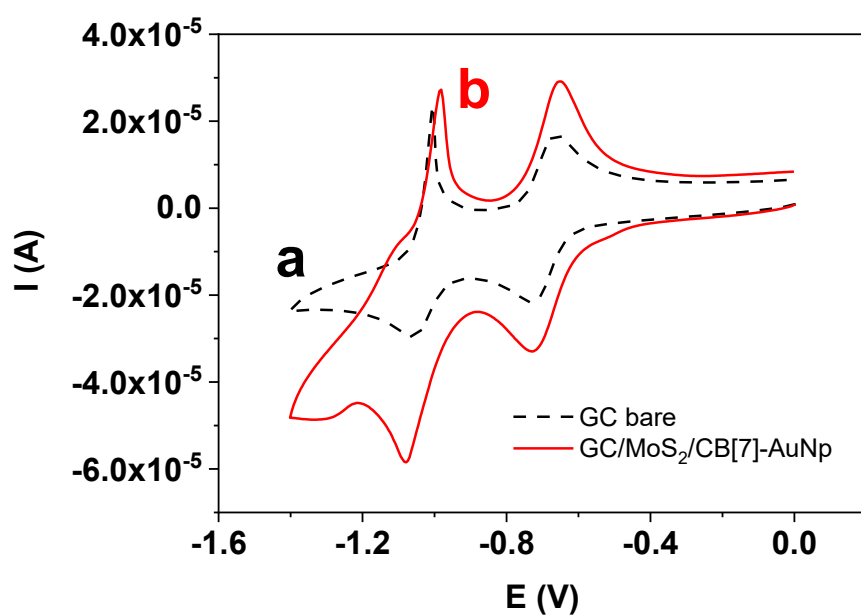


**Figure S1.** Cyclic voltammograms of 1.0 mM  $MV^{2+}$  recorded in 0.1 M phosphate buffer pH 7 at 100 mV/s. (a) Bare GC, (b) GC/MoS<sub>2</sub>/CB[7]-AuNp.

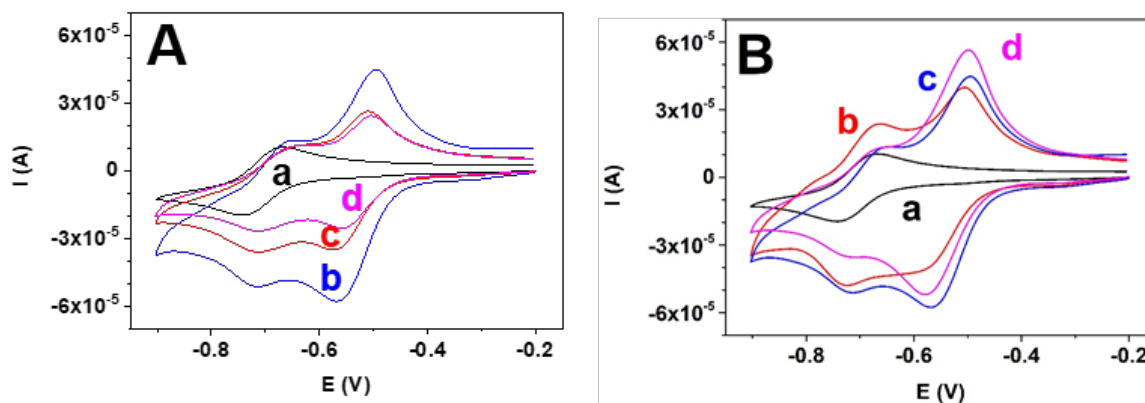


**Figure. S2.** Cyclic voltammograms of 1.0 mM  $MV^{2+}$  in 0.1 M phosphate buffer pH 7 at 100 mV/s recorded with the GC/MoS<sub>2</sub>/CB[8]-DNPs sensor. (A) Effect of the dilution of MoS<sub>2</sub> suspension: Bare GC (a) undiluted MoS<sub>2</sub> (b), diluted 1:5 (c) and diluted 1:10 (d). Sensor with 0.3 mM CB[8] concentration for the synthesis of CB[8]-DNPs. (B) Effect of the CB[8] concentration: Bare GC (a) and GC/MoS<sub>2</sub>/CB[8]-DNPs with undiluted MoS<sub>2</sub> and variable CB[8] concentration for the synthesis of CB[8]-DNPs, 0.1 (b), 0.3 (c) and 0.6 mM (d).

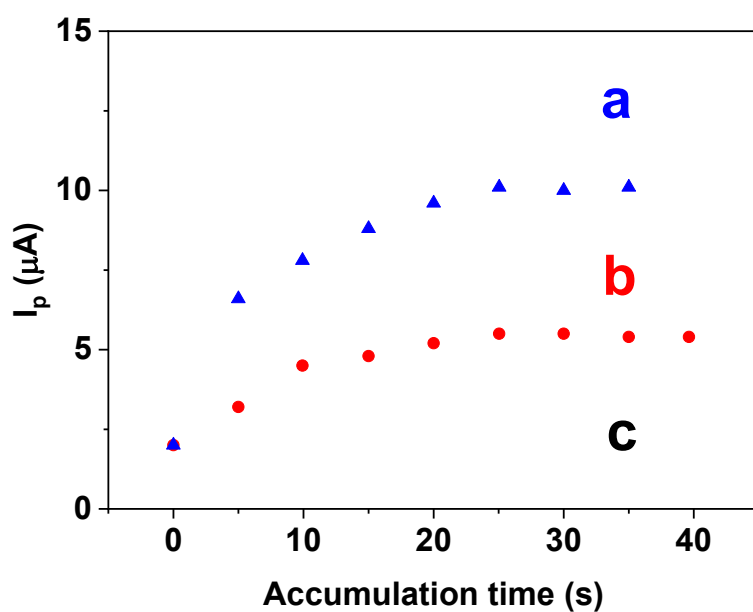


**Figure S3.** Effect of the accumulation time in the CB[8]-MV<sup>2+</sup> complex peak current with the sensor GC/MoS<sub>2</sub>/CB[8]-DNPs in 0.1 M phosphate buffer pH 7 at 7.5 (a), 5.0 (b) and 2.5 μM (c) MV<sup>2+</sup> concentrations. Eac= - 0.9 V, amplitude = 60 mV, scan rate = 30 mV/s.



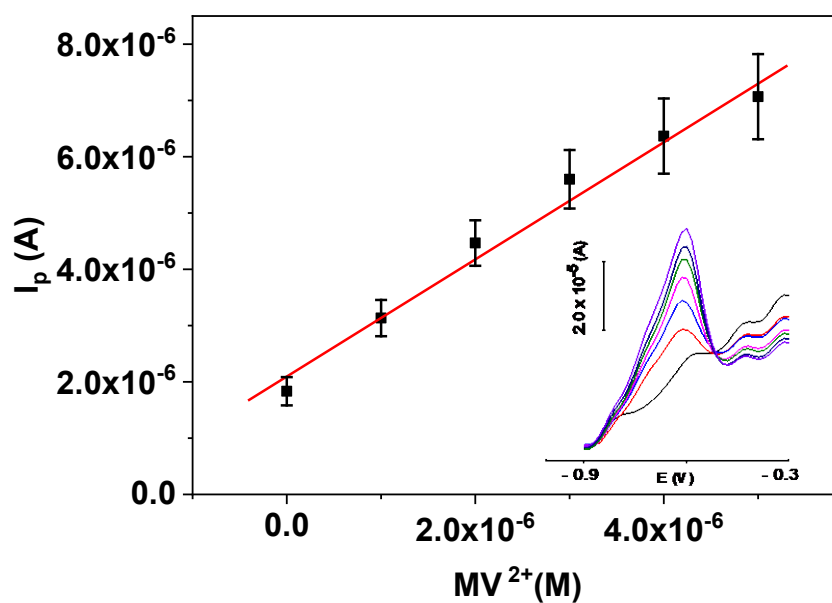


**Figure S4.** DPV analysis by standard addition procedure of a river water sample fortified at  $2.0 \cdot 10^{-5}$  M and diluted 1:10 in 0.1 M phosphate buffer pH 7 with the platform GC/MoS<sub>2</sub>/CB[8]-DNPs. Inset: Voltammograms of electrolyte (black line), 1:10 diluted fortified sample (red) and  $1.0 \cdot 10^{-6}$  to  $5.0 \cdot 10^{-6}$  MV<sup>2+</sup> standard additions.